STRESSES AND STRAINS AT ZIRCALOY CLADDING RIDGES

G. V. RANJAN, G. N. BROOKS

Failure Analysis Associates,
750 Welch Road, Suite 116, Palo Alto, California 94304, U.S.A.

A. K. MILLER

Department of Materials Science and Engineering,
Stanford University, Stanford, California 94305, U.S.A.

Ridges in Zircaloy claddings are formed or enhanced at pellet-pellet interfaces during a power increase, indicating strong pellet-clad mechanical interaction there. Most of the cladding failures by stress corrosion cracking (SCC) originate near the ridges. The present analysis is directed toward the determination of stress and strain distributions at the ridges, which will aid in studying the formation and growth of SCC cracks.

This paper decouples the behavior of fuel and cladding by assuming that the hourglassing of the pellet imposes highly localized loads on the cladding at pellet-pellet interfaces in addition to a uniform normal pressure and an axial force. These localized loads are not usually considered in most fuel rod codes. An elastic axisymmetric shell analysis of the cladding is done by asymptotic expansion method and closed form solutions are obtained. Since a typical cladding is fairly thick with a radius to thickness ratio of about 10, the effect of shear deformation is included. The following conclusions are reached: (1) smooth radial displacement profiles can be produced even by concentrated ring loads at ridges; (2) significant compressive axial stresses are present on the ID surface within 1 mm of the peak ridge position; these axial stresses become tensile further away from the ridge; (3) the maximum tensile circumferential stress is found at a short distance (about 1 mm) away from the ridge peak position and remains essentially uniform over a certain region (about 1 mm) on both sides of this maximum stress location; (4) the ratio of axial stress to circumferential stress varies with axial distance from the ridge; and (5) significant compressive axial stresses along with high tensile circumferential stresses produce high effective stresses at the ridges.

Subsequent to these elastic calculations, elastic-plastic analyses are done using STAGS, a finite difference shell code. The yield stress of irradiated Zircaloy is assumed to be 75 ksi (520 MPa) in these analyses. The cladding is loaded in steps and then unloaded so as to obtain the measured ridge height. For example, post-ramp profilometry measurements gave a maximum diametral ridge height of 0.5 mils for the Dresden-3 fuel rods. STAGS analysis for this situation calculated the maximum circumferential stress at the ID surface to be 70 ksi (480 MPa), whereas a typical fuel code with no ridging effect would have predicted a much lower stress (say, 25 ksi or less).

1. Introduction

Experience with Uranium Dioxide fuel with Zircaloy cladding has shown that a sudden power increase can, after a sufficient burn-up, lead to cladding failure. A power increase hourglasses the fuel pellet. In response to this thermal expansion of the pellet, the cladding deforms with ridges either formed or enhanced at pellet-pellet interfaces, indicating strong pellet-clad mechanical interaction (PCMI) there. In addition, the availability of fission products is maximum at the ridges, explaining the fact that most of the cladding failures by stress corrosion cracking (SCC) originate at or near the ridges. In the present investigation, stress and strain distributions at the ridges are determined, which will aid in studying the formation and growth of these SCC cracks. Bending effects are included in this study. However, the effects of thermal gradient, creep, and stress relaxation are not considered here.

Section 2.0 presents a simplified ridging model which decouples the behavior of fuel and cladding. This is done by assuming that hourglassing of the pellet imposes highly localized loads on the cladding at pellet-pellet interfaces in addition to a uniform normal pressure and an axial force everywhere. An elastic analysis of this axisymmetric ridging model is done by the asymptotic integration method [1], leading to closed form solutions for circumferential and axial stresses and strains. These elastic results in non-dimensional form are outlined in Section 3.0. Section 4.0 gives the elastic-plastic results for Dresden 3 and Maine Yankee fuel rods that either failed or had incipient cracks in them. These elastic-plastic analyses assume that the ridges measured for both the rods were formed only due to the power ramps which caused failures, and they were not enhanced due to any hydriding. Structural Analysis of General Shells (STAGS) [2], a specialized shell analysis computer program based on finite difference method and developed by Lockheed Palo Alto Research Laboratory, was used for this purpose. The uniaxial yield stress of irradiated Zircaloy [3] is assumed to be 75 ksi (520 MPa) in these analyses. Conclusions that emerged from these elastic-plastic analyses are presented in Subsection 4.3.

2. Ridging Model

2.1 Assumptions

During a power ramp, the pellet assumes an hourglass shape. Consequently, the ends of adjacent pellets will tend to deform the cladding so as to create a circumferential ridge. The forces exerted by the pellet on the cladding are approximated by uniform normal pressure and axial force everywhere in the cladding and highly localized loads at pellet-pellet interfaces. These localized loads are not usually considered in most fuel rod codes.

The pellet may crack longitudinally due to the radial thermal gradient developed during the power ramp, rendering the normal force distributions to be non-axisymmetric. In addition, interfacial friction forces in the circumferential direction would be imposed on the cladding. The stress distributions due to these forces and their implications on SCC crack formation and growth are already discussed in Ref. [4]. In the present approach, it is assumed that no radial pellet cracks form. Hence, the circumferential frictional forces are not included. Also, the normal forces are considered to be axisymmetric. As the pellets change their volume and shape, they may also exert frictional forces on the cladding in the axial direction. These are not considered in the present model. In addition, it is assumed

that any two adjacent pellets have the same behavior, and, hence, the force distribution and deformation are symmetric with respect to the pellet end cross-section. For pellets with large length to diameter (L/D) ratios, transverse cracks are expected to form or get enhanced at mid-pellet section during a power ramp, thus, imposing localized loads on the cladding there as at the pellet-pellet interfaces. Most SCC cracks initiate in the vicinity of the primary ridges (ridges at pellet-pellet interfaces) and the secondary ridges (ridges at mid-pellet sections). Hence, only the local stress and strain distributions at these ridges are needed to study the formation and growth of these cracks. As the bending stresses and strains due to the localized loads at primary ridges decay much before the adjacent secondary ridges and vice versa, the two types of ridges can be decoupled and analyzed separately.

2.2 Simplified Models

Figure 1 illustrates the ridge models which incorporate these assumptions. In Fig. 1a, the localized loads are taken to be concentrated ring loads at the ridge location. Elastic results are determined only for this model. Elastic-plastic analysis is done for both the models shown in Figs. 1a and 1b. Figure 1b assumes that the ring load is applied slightly away from the ridge to consider the fact that due to hourglassing the outer edges of two adjacent pellet ends are not in contact but separated by a short distance. In reality, the load is distributed locally at the ridge. Hence, this case lies between the two extreme situations shown in Figs. 1a and 1b and needs to be analyzed only if the stress and strain distributions for the two extreme loading cases differ substantially.

The Danish code WAFER [5] considers the effect of localized loads at ridges using linear bending theory for thin shells. However, it appears that only the membrane stresses (i.e., no bending stresses) are computed. The code COMETHE-IIIK [6] analyzes the ridge by having a thin dummy slice in the pellet at the ridge location with a larger coefficient of thermal expansion than the rest of the pellet. However, it does not consider the bending effects.

3. Elastic Solution by Asymptotic Integration Method

3.1 Membrane Solution

The cladding is considered to be in a generalized plane strain condition with uniform normal pressure P and axial stress resultant V acting as shown in Fig. 1a, where $P = P_{PCMI} + P_f - P_c$ with P_{PCMI} being the average contact pressure due to PCMI, as calculated by a typical one-dimensional fuel rod code; P_f being the fission gas pressure; and P_c being the coolant pressure. From the axial and normal equilibrium of the cladding, the axial and circumferential stresses are

$$\sigma_{z,m} = V/t$$
$$\sigma_{\theta,m} = PR/t \qquad (1)$$

where subscript m denotes membrane solution. These stresses are related to the axial and circumferential strains, $\varepsilon_{z,m}$ and $\varepsilon_{\theta,m}$ developed during the power ramp as follows:

$$\sigma_{z,m} = \frac{E}{1 - \nu^2} (\varepsilon_{z,m} + \nu\varepsilon_{\theta,m}) \qquad (2)$$

and

$$\sigma_{\theta,m} = \frac{E}{1 - \nu^2} (\sigma_{\theta,m} + \nu\varepsilon_{z,m}) \qquad (3)$$

where E and ν are the Young's modulus and Poisson's ratio of cladding material. The stress and strain ratios are now defined as $\gamma = \sigma_{z,m}/\sigma_{\theta,m}$ and $\beta = \varepsilon_{z,m}/\varepsilon_{\theta,m}$, where β is strongly dependent on the power ramp size, ramp rate, and pellet geometry. For fast power ramps on fuel rods with flat ended pellets, β can be as high as 2.0, whereas, for slow power ramps on dished pellets, β can be as low as 0.0 [7]. Using Eqs. (2) and (3), these ratios can be related as

$$\gamma = \frac{\beta + \nu}{1 + \beta\nu} \tag{4}$$

Knowing the average radial thermal expansion of the pellet and, hence, the circumferential strain $\varepsilon_{\theta,m}$ as well as the axial strain $\varepsilon_{z,m}$ developed in the cladding during a power ramp using a one-dimensional fuel rod code, the membrane stresses are easily calculated using Eqs. (2) and (3). These, in turn, give the normal pressure P and axial stress resultant V through Eq. (1), that are to be input in the elastic-plastic analyses described in Section 4.0.

3.2 Bending Solution for Ring Loads

3.2.1 Geometric Nonlinear Effect

The change in the meridional slope can be an important geometric nonlinearity. It was shown in Ref. [8] that even for severe power ramps, the geometric nonlinear effect is small and, hence, is neglected in the present ridging calculations.

3.2.2 Solution With Shear Deformation Effect

Figure 2 shows the cladding with a ring load applied at the ridge. Due to symmetry, only the upper half of the shell is analyzed. We now define the variable vector $\bar{y}$, which has for its components the physical variables which can be prescribed at an edge of a cylindrical shell as shown in Fig. 2: the meridional moment resultant M_z, the radial stress resultant H, the rotation χ, and the radial displacement h,

$$\bar{y} = \begin{bmatrix} y_1 \\ y_2 \\ y_3 \\ y_4 \end{bmatrix} = \begin{bmatrix} M_z/Etc \\ H\lambda/Et \\ \chi/\lambda \\ h/R \end{bmatrix} \tag{5}$$

where $\lambda = (R/c)^{1/2}$ and $c = t\left[12(1 - \nu^2)\right]^{-1/2}$, the reduced thickness. The boundary conditions at the ridge are shown in Fig. 2.

The radius to thickness ratio (R/t) for a typical cladding can be as low as 7. Hence, thin shell theory is not directly applicable to analyze such fairly thick claddings. However, it was shown in Ref. [8] that if the effect of shear deformation is included in the thin shell theory equations, then thick clads can be analyzed accurately.

The solution vector which provides stresses and strains as a function of arc length S from the edge is written as [9]

$$\bar{y} = \mathrm{Re}\left\{ C \begin{bmatrix} e^{-i\eta} \\ e^{-i\eta/2} \\ e^{-i3\eta/2} \\ 1 \end{bmatrix} e^{\lambda\xi} \right\} \tag{6}$$

where $\lambda\xi = -(\cos\eta/2 + i\sin\eta/2)y$ with $y = |S|/\sqrt{cR}$ and $\cos\eta = \mu/2\lambda^2$, where the parameter μ defines the effective transverse shear modulus as $G = E/\mu$, and it includes the effect of shear deformation. For Zircaloy cladding, μ may take a value of about 3.0.

Evaluating the complex constant C using the boundary conditions and introducing the variable $x = (\sin\eta/2)y$, the stresses and strains on the ID surface of the cladding due to ring load alone are determined as

$$\varepsilon_{\theta,ID} = \varepsilon_{\theta,Direct} = \frac{h}{R} = \frac{h_o}{R}\, e^{-(\cos\eta/2)y}\left(\cos x - \cot\frac{3\eta}{2}\sin x\right) \tag{7}$$

$$\varepsilon_{z,ID} = \begin{cases} \varepsilon_{z,Direct} - |\varepsilon_{z,Bending}| \\ -\nu\varepsilon_{\theta,Direct} - M_z/(2Ec^2) \end{cases} \tag{8}$$

where

$$\frac{M_z}{2Ec^2} = \frac{h_o}{R} \times \left[3(1-\nu^2)\right]^{1/2} \times e^{-(\cos\eta/2)y} \times \left\{(\cos\eta\cos x - \sin\eta\sin x) - \cot\frac{3\eta}{2}(\cos\eta\sin x + \sin\eta\cos x)\right\}$$

$$\sigma_{\theta,ID} = \begin{cases} \sigma_{\theta,Direct} - |\sigma_{\theta,Bending}| \\ E\varepsilon_{\theta,Direct} - \nu|\sigma_{z,Bending}| \end{cases} \tag{9}$$

where

$$|\sigma_{z,Bending}| = \frac{6M_z}{t^2} = \frac{Eh_o}{R} \times \left(\frac{3}{1-\nu^2}\right)^{\frac{1}{2}} \times e^{-(\cos\eta/2)y} \times \left\{(\cos\eta\cos x - \sin\eta\sin x) - \cot\frac{3\eta}{2}(\cos\eta\sin x + \sin\eta\cos x)\right\}$$

$$\sigma_{z,ID} = -|\sigma_{z,Bending}| \tag{10}$$

where h_o is the radial displacement at the ridge due to the ring load alone. For the case of $\mu = 0$, so that $\eta = \pi/2$, these stresses and strains are plotted as a function of dimensionless arc length $z = y/\sqrt{2}$ in Figs. 3 through 5 in Ref. [8].

3.2.3 Boundary Layer Thickness

The boundary layer thickness in a shell of revolution is defined as the distance from the ridge at which location the stresses and strains decay to negligible fraction of the edge value (for example, a fraction of $e^{-\pi}$). For axisymmetric loading on a cylindrical shell, the boundary layer thickness δ is given as

$$\delta = \pi\sqrt{2Rc} \tag{11}$$

If L and D are the length and diameter of the cladding, respectively, then

$$\frac{\delta}{L} = \pi\left(\frac{D}{L}\right)\left(\frac{t}{2R\sqrt{12(1-\nu^2)}}\right)^{1/2} \tag{12}$$

For a cladding with $R/t = 10$ and $\nu = 0.35$, the boundary layer thickness becomes $\delta/L = 0.39(D/L)$. For $L/D = 1$, $\delta/L = 0.39$. If secondary ridges do not form at the mid-pellet section (i.e., at arc length $S = L/2$ in Fig. 2), then the bending solutions due to two adjacent primary ridges are

uncoupled. Even if secondary ridges form, the primary and the adjacent secondary ridges can be analyzed independent of each other. However, to obtain the stresses and strains from $S/L = 0.11$ to $S/L = 0.39$ for this cladding, the contributions from both these ridges have to be superimposed. For $L/D = 1.5$, $\delta/L = 0.26$, and, hence, there is complete uncoupling between primary and secondary ridges.

3.2.4 Half-Width of the Ridge

Half-width of a ridge is defined as the distance from the ridge (i.e., $S = 0$ in Fig. 2) to the location where the radial displacement due to ring load becomes zero. In other words, it is the distance at which $\varepsilon_{\theta,\text{Direct}}$ becomes zero. From Eq. (7), it is seen that the half-width of an elastic ridge is approximately three-fourths of the boundary layer thickness. This indicates that even for the extreme situation of concentrated ring load at the ridge, the radial displacement profile is smooth. Hence, it is difficult to predict from the shape of clad profile whether the load applied is concentrated like a ring load at the ridge or distributed over a band width with maximum occurring at the interface.

3.3 Stress Distribution at the Ridge

Adding the membrane and bending solutions presented in the previous two subsections, the axial and circumferential stresses on the cladding ID surface are determined as

$$\sigma_{z,ID} = \frac{(\beta + \nu)\, E\varepsilon_{\theta,m}}{(1 - \nu^2)} - \sigma_{z,\text{Bending}} \tag{13}$$

$$\sigma_{\theta,ID} = \frac{(1 + \beta\nu)\, E\varepsilon_{\theta,m}}{(1 - \nu^2)} + E\varepsilon_{\theta,m}\,(\alpha - 1) \times e^{-(\cos\eta/2)y}\left(\cos x - \cot\frac{3\eta}{2}\sin x\right) - \nu\sigma_{z,\text{Bending}} \tag{14}$$

where

$$\sigma_{z,\text{Bending}} = E\varepsilon_{\theta,m}\,(\alpha - 1)\left(\frac{3}{1 - \nu^2}\right)^{1/2} \times e^{-(\cos\eta/2)y}\left\{(\cos\eta\cos x - \sin\eta\sin x) - \cot\frac{3\eta}{2}\,(\cos\eta\sin x + \sin\eta\cos x)\right\}$$

and α = total radial ridge height/$(R\varepsilon_{\theta,m})$.

The term $R\varepsilon_{\theta,m}$ is the average radial expansion as calculated by one-dimensional fuel rod modelling codes. Hence, $\varepsilon_{\theta,m}(\alpha - 1)$ is the circumferential strain at the ridge produced by the ring load alone. The von Mises effective stress for a shell of revolution undergoing axisymmetric deformation is defined as

$$\sigma_{eff} = (\sigma_z^2 + \sigma_\theta^2 - \sigma_z\sigma_\theta)^{1/2} \tag{15}$$

The dimensionaless form of these stresses for different values of α and β are shown in Figs. 3 through 6. The parameter $\beta = 0$ corresponds to global plane strain condition, and $\beta = 2$ corresponds to the situation that would occur for a fast power ramp on fuel rods with flat ended pellets completely locked to cladding. The parameter α provides a measure of severity of ridge enhancement during a ramp. Yield occurs when σ_{eff} reaches uniaxial yield stress.

3.4 Conclusions From Elastic Calculations

The following conclusions are reached from the elastic calculations presented in this Section.

(1) Smooth radial displacement profiles can be produced even by concentrated ring loads at ridges.

(2) Significant compressive axial stresses are present on the ID surface within a short distance from the peak ridge position for small values of β (Fig. 3). However, for large values of β (Fig. 4), the axial stresses are tensile everywhere in the cladding.

(3) The tensile mid-surface circumferential stress is maximum at the ridge peak position and decays away from it. On the other hand, the circumferential bending stress is compressive on the ID at the ridge and becomes tensile away from it. Hence, the total stress on the ID surface takes the distribution shown in Figs. 3 and 4. Although the total stress peaks at a short distance away from the ridge peak position, it remains essentially uniform over a certain region on both sides of its peak position.

(4) The ratio of axial stress to circumferential stress varies strongly with axial distance from the ridge.

(5) The effective stress peaks at the ridge and decays to the nominal value for small values of β (Fig. 5). For larger β (Fig. 6), it peaks at the ridge only when fairly severe ridges (with large height) are formed.

4. Elastic-Plastic Analyses of Dresden-3 and Maine Yankee Fuel Rods

4.1 Description of Rods

To evaluate the stresses and strains developed due to pellet-cladding interaction (PCI) on BWR fuel, Dresden-3 fuel rods were selected. These rods experienced an inadvertent transient power increase that resulted in failures. The results of nondestructive and destructive examinations carried out in these rods are presented in Ref. [10]. For the purpose of obtaining detailed stress and strain distributions at the ridges, the Rod KE-2225 is chosen here. A maximum diametral ridge height of 0.013 mm (0.5 mils) was measured on this rod [11], which contained dished pellets. Dimensions of this rod are [12]: (1) Pellet Length, L = 0.84 inch (2.13 cm); (2) Mid-Surface Radius of Cladding, R = 0.2655 inch (6.745 mm); and (3) Cladding Thickness, t = 0.032 inch (0.81 mm). The material properties for the irradiated Zircaloy-2 cladding are [3]: (1) Young's Modulus, $E = 11.5855 \times 10^6$ psi (79.9×10^3 MPa); (2) Poisson's Ratio, $\nu = 0.348$; and (3) Yield Stress, $\sigma_y =$ 75,000 psi (520 MPa). The material is taken to be elastic-perfectly plastic with no strain hardening. The boundary layer thickness δ for this rod as given by Eq. (11) equals 0.227 inch (5.77 mm). As the power transient is fairly strong, the dishes were filled and the pellets seemed to be in contact at the center of the dishes. This could be expected to lead to fairly strong axial interaction. Such axial extensions were observed in this rod [10]. We, therefore, picked a reasonable, but somewhat arbitrary value of 0.8 for β ($= \varepsilon_{z,m}/\varepsilon_{\theta,m}$). A better estimate for β may be obtained by using codes such as COMETHE-IIIK [6]. It is also assumed that calculations using a one-dimensional fuel rod modelling code provide the membrane result for the circumferential stress $\sigma_{\theta,m}$ to be 10,000 psi (70 MPa). Knowing β and $\sigma_{\theta,m}$, the net pressure P and the axial stress resultant V can be calculated using Eqs. (1) and (4), which are necessary inputs for the elastic-plastic analyses of both the ridging models shown in Fig. 1. The distance d in Fig. 1b is taken to be 0.024 inch (0.6 mm).

An additional loading situation with $\sigma_{\theta,m} = 25{,}000$ psi (173 MPa) and ring load at the ridge was also analyzed for this rod and the results are given in Ref. [8]. Comparison of

these results with those for the case with $\sigma_{\theta,m}$ = 10,000 psi showed that the residual radial displacement profile as well as the locations of the maximum tensile axial and circumferential stresses do not change with the membrane circumferential stress assumed. However, the magnitudes of the stresses differ by as much as the difference in their membrane solutions.

To evaluate the local ridging effects in PWR fuels, Fuel Rod JBY-097, which was in Maine Yankee Core I, was selected. Complete description of the Fuel Performance Evaluation Program on the Maine Yankee Core I fuel rods is given in Ref. 13 . Linear diameter traces measured a maximum ridge height of 0.4 mil (0.0102 mm) for this rod. Reference 13 provides the following data for the elastic-plastic analysis: (1) Pellet Length, L = 0.6452 inch (16.388 mm); (2) Mid-Surface Radius of Cladding, R = 0.207 inch (5.258 mm); (3) Cladding Thickness, t = 0.026 inch (0.66 mm); and (4) Boundary Layer Thickness, δ = 0.18 inch (4.572 mm). In the present analysis, the irradiated cladding material (Zircaloy-4) is assumed to be elastic-perfectly plastic with no strain hardening and with the same properties as for the Dresden-3 Rod KE-2225. Although the actual power changes in the Maine Yankee Core I, which triggered the pellet-clad interaction, were small, the temperature change experienced by the fuel was equivalent to that normally associated with a larger power change. As the pellets were also dished, the membrane circumferential stress $\sigma_{\theta,m}$ and β are assumed to be $\sigma_{\theta,m}$ = 10,000 psi (70 MPa) and β = 0.5 for this power ramp. Better estimates may be obtained using a fuel rod modelling computer code. The ring load is applied only at the ridge of this rod.

4.2 Method of Analysis

Elastic-plastic analysis is done using STAGS. The code is based on a theory which combines energy principles and finite difference methods. The theory includes the two important geometric nonlinearities due to prestress and moderately large rotation. However, shear deformation effect is not included. Yielding is according to von Mises and for axisymmetric loading it becomes $\sigma_1^2 - \sigma_1\sigma_2 + \sigma_2^2 + \sigma_y^2$, where σ_1 and σ_2 are the axial and circumferential stresses.

For the STAGS analysis, the boundary layer thickness of the ridging models shown in Figs. 1a and 1b is broken into fine finite difference mesh, while the rest of the cladding is divided into coarse mesh. Symmetry is imposed at S = 0, while axial stress resultant V is applied at S = L/2. The edge S = L/2 is also constrained from having any rotation. Net internal pressure P is prescribed everywhere in the cladding, and both V and P are kept constant, while the ring load is increased in steps at the appropriate location (i.e., at S = 0 for model shown in Fig. 1a and at S = d for the one in Fig. 1b). The ring load, P and V, are then unloaded simultaneously to obtain the measured ridge height.

4.3 Conclusions From Elastic-Plastic Analyses

The results for the two loading cases for the Dresden-3 Rod KE-2225 are compared in Figs. 7 through 10. Only ID surface stresses are plotted in these figures. Conclusions reached from these analyses are now summarized.

(1) A ring load alone is sufficient to develop smooth ridge profiles seen in profilometry traces.

(2) Location of the ring load (i.e., either at the ridge or at a short distance from the ridge) has only marginal effect on the residual displacement profile and has negligible effects on stress distributions everywhere in the cladding except at the ridge. Hence, an analysis of the ridging model where the load is distributed locally at the

ridge, would not provide any new information. In addition, analysis of the ridging model with ring load at the ridge (Fig. 1a) is sufficient to accurately determine the stress and strain distributions everywhere in the cladding. Hence, only this model is analyzed for the Maine Yankee Rod JBY-097.

(3) The maximum tensile axial stress occurs at a distance of half the boundary layer thickness from the ridge and could be as high as 55% of the yield stress. And the maximum tensile circumferential stress occurs at about one-fourth of the boundary layer thickness and could be as high as 85% of the yield stress. A typical fuel code with no ridging effect would have predicted only stresses as high as 15% of yield stress.

(4) The circumferential stress alone is not sufficient to yield the cladding. It is the compressive axial stress that is responsible for the cladding to yield at the ridge. However, if the effect of creep is included, then the ridge will be formed mainly under the influence of circumferential stress.

(5) The axial stress to circumferential stress ratio changes rapidly with axial distance.

The residual radial displacement profile and the axial and circumferential stress distributions for the Maine Yankee Rod JBY-097 take the same shape as those for the Dresden-3 Rod KE-2225 and, hence, are not presented here. However, they are shown in Figs. 18 through 21 in Ref. (8). The axial distribution of effective stress and the variation of circumferential stress through the thickness at the axial location, where the tensile circumferential stress at the ID surface is maximum, are shown in Figs. 11 and 12. Additional conclusions reached from these figures are:

(6) The plastic zone is very localized and extends only up to a distance of one-eighth of the boundary layer thickness.

(7) The circumferential stress gradient through the thickness is small.

Because of the assumption in these analyses that the material is elastic-perfectly plastic with no creep, the ridges are formed only when the cladding yields. Also, these analyses indicate that at any ridge, the circumferential stress is as high as the yield stress. However, if creep is included in the above calculations, then ridges could be formed at stresses much below the yield stress. The authors are presently investigating the effect of creep on the stress and strain distributions at ridges.

REFERENCES

/1/ Ranjan, G. V., "Edge Zone Expansions for Thin Shells With Application to (1) Torispherical Pressure Vessel and (2) Large Deflection of Sphere With Point Load," Ph.D. Dissertation, Stanford University, Stanford, CA (November 1976).

/2/ "Structural Analysis of General Shells, User Instructions for STAGSC," Vol. 3, Lockheed Palo Alto Research Laboratory, Palo Alto, CA (December 1975).

/3/ Bauer, A. A., L. M. Lowry, and J. F. Perrin, "Evaluating Strength and Ductility of Irradiated Zircaloy," Battelle-Columbus Report No. BMI-NUREG-1976 (July 1977).

/4/ Miller, A. K., et al., "Zircaloy Cladding Deformation and Fracture Analysis," EPRI Interim Report No. NP-856, Projects 700/961 (August 1978).

/5/ Kjaer-Pedersen, N., "A New Version of the LWR Fuel Performance Model, WAFER," Proceedings 4th International SMiRT Conference, Paper D1/3, San Francisco, CA (August 1977).

/6/ Hoppe, N., "COMETHE-IIIK With PCMI Improvements," To be presented at the 25th Annual ANS Meeting, Atlanta, GA (June 1979).

/7/ Hoppe, N., "Improvements to COMETHE-IIIJ Fuel Rod Modeling Code," IAEA Specialists Meeting on Fuel Element Performance Computer Modeling, Blackpool, UK (March 1978).

/8/ Miller, et al., "Zircaloy Cladding Deformation and Fracture Analysis," Third Quarterly Progress Report, EPRI Project RP-971 (December 1978).

/9/ Fettahlioglu, O. A. and C. R. Steele, "Asymptotic Solutions for Orthotropic Nonhomogeneous Shells of Revolution," J of Appl Mechanics, Trans ASME (September 1974), Pp. 753-758.

/10/ Pasupathi, V., et al., "Determination and Microscopic Study of Incipient Defects in Irradiated Power Reactor Fuel Rods," EPRI Final Report No. NP-812, Project 829 (July 1978).

/11/ Pasupathi, V., et al., "Determination and Microscopic Study of Incipient Defects in Irradiated Power Reactor Fuel Rods," Battelle Interim Report No. BCL-585-1 (August 1977).

/12/ Rosenbaum, H. S., "Data Package for BWR Fuel Rods Selected for Study in the Program 'Determination and Microscopic Study of Incipient Defects in Irradiated Power Reactor Fuel Rods,'" Vol. 1, General Electric Report NEDC-23557 (March 1977).

/13/ Fuhrman, N., et al., "Evaluation of Fuel Rod Performance in Maine Yankee Core I," EPRI Final Report No. NP-218, Project 586-1 (November 1976).

ACKNOWLEDGEMENTS

This research was sponsored by the Electric Power Research Institute, Palo Alto, California. The authors are thankful to several colleagues, particularly to Drs. E. Smith, N. Hoppe, and Dr. J. T. A. Roberts for valuable discussions throughout the work.

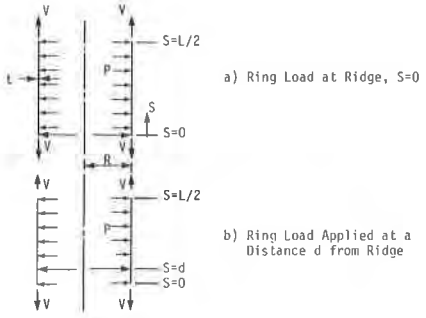

a) Ring Load at Ridge, S=0

b) Ring Load Applied at a Distance d from Ridge

Figure 1 - Simplified Ridging Models With S Being the Arc Length, L the Pellet Length, R the Midsurface Radius of Cladding, P the Net Pressure, V the Axial Stress Resultant, and t the Cladding Thickness.

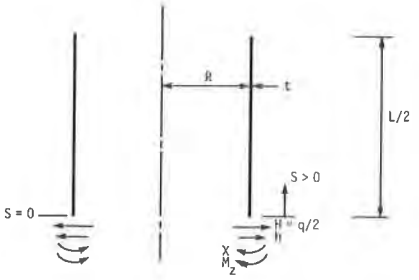

Symmetry condition X = 0 and H = q/2 imposed at ridge location, S = 0, where q is the ring load

Figure 2 - Edge Forces and Edge Displacement at Ridge.

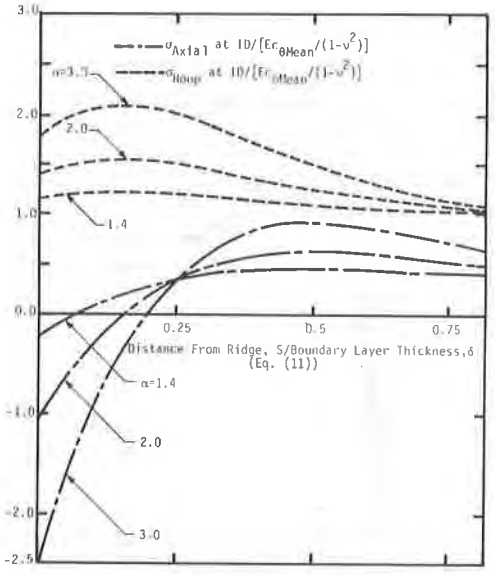

Figure 3 - Elastic Results for Axial and Circumferential Stresses At Cladding I.D. Surface for β = 0.

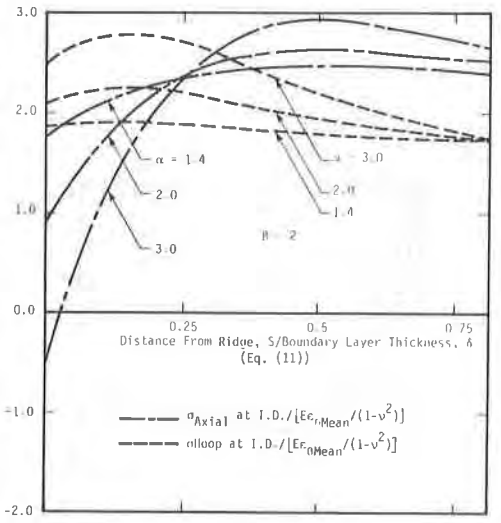

Figure 4 - Elastic Results for Axial and Circumferential Stresses at Cladding I.D. Surface for β = 2

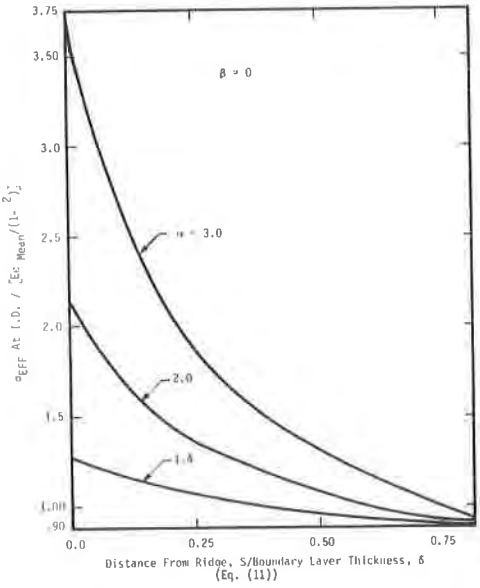

Figure 5 - Effective Stress at Cladding I.D. Surface for β = 0. (Elastic Analysis).

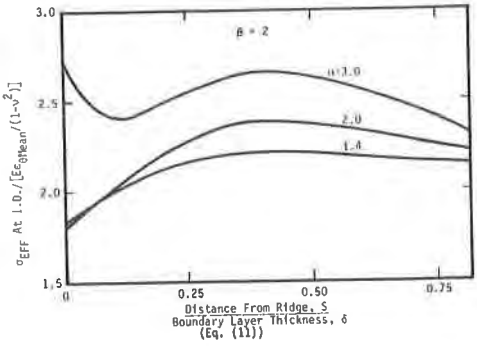

Figure 6 - Effective Stress at Cladding I.D. Surface for β = 2 (Elastic Analysis).

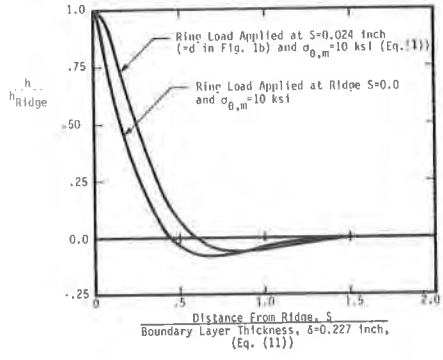

Figure 7 - Comparison of Residual Radial Displacement Profiles for Two Loading Conditions for Dresden-3 Rod KE2225.

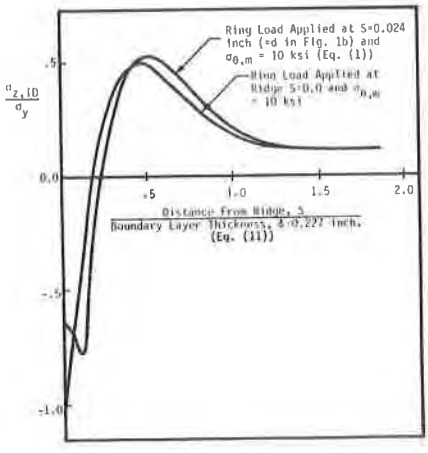

Figure 8 - Comparison of Axial Stress Distributions for Two Loading Conditions for Dresden-3 Rod KE2225.

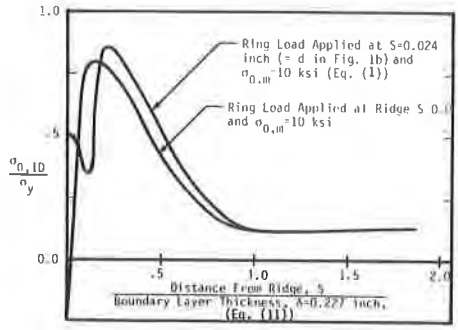

Figure 9 - Comparison of Circumferential Stress Distributions for Two Loading Conditions for Dresden-3 Rod KE2225.

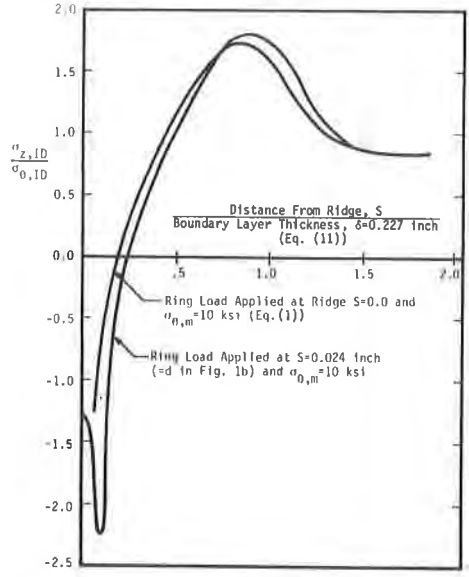

Figure 10 - Comparison of Axial Stress to Circumferential Stress Ratios for Two Loading Conditions for Dresden-3 Rod KE2225.

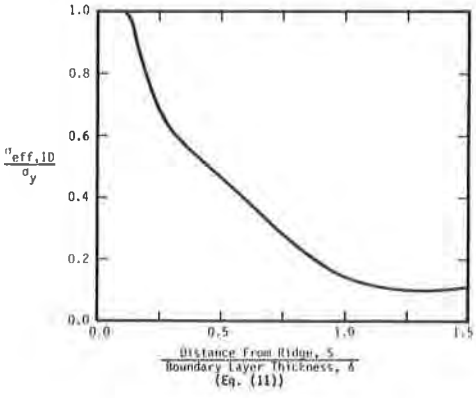

Figure 11 - Effective Stress Distribution for Maine Yankee Fuel Rod JBY-097.

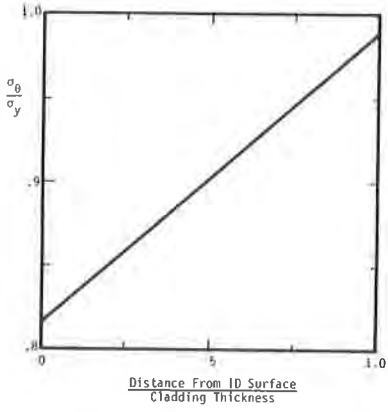

Figure 12 - Variation of Circumferential Stress Through the Cladding Thickness at Axial Location Where Circumferentail Stress is Maximum on the ID Surface for Maine Yankee Rod JBY-097